Mitochondrial Ultrastructure Is Coupled to Synaptic Performance at Axonal Release Sites

Csaba Cserép[1,2,*] Balázs Pósfai[1], Anett Dóra Schwarcz[1], Ádám Dénes[1,*]

[1]*Momentum* Laboratory of Neuroimmunology, Institute of Experimental Medicine, Hungarian Academy of Sciences, Szigony U. 43, Budapest 1083, Hungary.

[2]Lead contact

*Correspondence: cserep.csaba@koki.mta.hu, denes.adam@koki.mta.hu

SUMMARY

Mitochondrial function in neurons is tightly linked with metabolic and signalling mechanisms that ultimately determine neuronal performance. The subcellular distribution of these organelles is dynamically regulated as they are directed to axonal release sites on demand, but whether mitochondrial internal architecture and molecular properties would reflect the actual performance requirements in a synapse-specific manner, remains to be established. Using electron-tomography and super-resolution microscopy, we examined performance-determining ultrastructural features of presynaptic mitochondria in GABAergic and glutamatergic axons. These features were coupled to synaptic strength: mitochondria in boutons with high synaptic activity exhibited an ultrastructure optimized for high rate metabolism and contained higher levels of the respiratory chain protein cytochrome-c than mitochondria in boutons with lower activity. The strong, cell-type independent correlation between mitochondrial nano-architecture, molecular fingerprints and synaptic performance suggests that changes in synaptic activity could trigger ultrastructural plasticity of presynaptic mitochondria, likely to adjust their performance to the actual metabolic demand.

KEYWORDS: mitochondria, crista, synapse, cytochrome-c, hippocampus, electron-tomography, super-resolution microscopy

INTRODUCTION

About one-tenth of total grey matter volume is occupied by mitochondria, the powerhouses of cells (Toussaint and Kugler, 1989). These organelles form a rapidly changing, dynamic network in neurons (Barnhart, 2016). As primary energy generators, precise regulation of mitochondrial performance is fundamental for proper functioning of the central nervous system (CNS), due to the exceptionally high ATP-consumption of neuronal tissue. Mitochondria are also key regulators of intracellular calcium levels (Gunter et al., 2000; Hall et al., 2012) and contribute to signalling processes, the regulation of cell proliferation, migration, neuronal morphology and cell viability (Chandel, 2014). Since the main energy consumer in the CNS is synaptic transmission (Harris et al., 2012), intact mitochondrial ATP-production – together with calcium-regulation – is crucial for proper synaptic function and neuroplasticity (Billups and Forsythe, 2002; Gazit et al., 2016; Smith et al., 2016; Verstreken et al., 2005). Furthermore, the availability of presynaptic mitochondria at axonal release sites directly influences synaptic function (Rangaraju et al., 2014; Smith et al., 2016; Sun et al., 2013).

In highly dynamic neuronal networks cellular morphology and synaptic strength is changing in an activity dependent manner (Muller et al., 2002), resulting in altered neuronal demand for mitochondrial supply in space and time. Recent data also suggest that mitochondrial distribution within neurons is dynamically regulated to match the actual needs. *In vitro* studies confirmed, that motile mitochondria in dendrites as well as in axons are recruited and anchored to synapses whenever the local need for mitochondrial performance increases (Li et al., 2004; Sheng, 2014). It has also been shown in non-neuronal tissues that the inner nano-architecture of mitochondria determines their output performance. The surface area of crista-membrane (CM) in a given mitochondrial volume strongly correlates with mitochondrial oxygen consumption and cytochrome-oxidase activity (Else et al., 2004; Perkins et al., 2012, 2003; Sood et al., 2014). In addition to CM-density, the shape of cristae has also been shown to directly regulate mitochondrial performance output (Cogliati et al., 2013), and influence mitochondrial Ca^{2+}-dynamics (Mannella et al., 2013).

Based on these data, we hypothesized that the nano-architecture of these organelles may be structured to match the actual local needs in neurons. To test this idea with high-resolution imaging, we performed electron tomography and STORM super-resolution microscopy studies on mouse brain tissues, combined with serial-section transmission electron microscopy studies on post-mortem human tissue samples. We examined presynaptic mitochondria in GABAergic and glutamatergic axons of the hippocampal formation. We found that CM-density, crista tightness and cytochrome-c density was higher in presynaptic

mitochondria of the highly active fast-spiking parvalbumin-positive (PV) basket cells than in the mitochondria of the slow firing type-1 cannabinoid receptor-positive (CB1R) basket cells, which are the well characterized archetypes of high-activity and low-activity interneurons, respectively. We also examined presynaptic mitochondria in the glutamatergic boutons of the perforant-path terminating zone in the dentate gyrus, and found a strong, cell-type independent correlation between mitochondrial volume, CM-density, crista tightness, cytochrome-c density and synaptic strength. The results from human post-mortem tissue also confirmed that this phenomenon is evolutionally conserved. Our data provide evidence for the logical assumption, that "stronger synapses use stronger mitochondria", and point out the possibility of the activity-dependent ultrastructural plasticity of these organelles.

RESULTS

Electron tomography reveals robust ultrastructural differences between presynaptic mitochondria of fast-spiking and regular-spiking GABAergic neurons

In order to test whether any correlation exists between synaptic performance and mitochondrial ultrastructure, we defined a "low performance" and a "high performance" group within hippocampal GABAergic as well as glutamatergic synaptic populations, based on the level of their activity. In the hippocampal CA1 area, the perisomatic GABAergic inputs of principal cells can be divided into two, morphologically and functionally well-characterized populations: the CB1R-positive, regular-spiking interneurons show low level of synaptic activity, whereas the PV-positive, fast-spiking interneurons are capable of performing exceptionally high synaptic activity. In fact, these GABAergic populations are the two well-known archetypes of the slow/modulatory, and the highly energized/fast "clockwork" type interneurons, respectively (Gulyás et al., 2006; Kann et al., 2014; Klausberger et al., 2005). The average *in vivo* firing frequency of the CB1R+ interneurons in the hippocampus is 2-10 Hz, whereas the PV+ interneurons can fire bursts up to 150 Hz during ripples (Klausberger et al., 2005; Lapray et al., 2012), making these two populations ideal candidates for "low performance" (LP) and "high performance" (HP) GABAergic boutons, respectively. Since the perisomatic synaptic boutons contacting pyramidal cells in the hippocampal CA1 region originate exclusively (99%) from these two cell types (Takács et al., 2015), labeling one of them is sufficient to reliably identify both types. To verify the exclusive and non-overlapping contribution of the two populations with our antibodies as well, we performed immunofluorescent labeling of GABAergic varicosities for vesicular GABA transporter (vGAT), the two bouton-populations for CB1R and PV, and cell nuclei with DAPI (Fig. 1., A). We found, that 54.5% of all GABAergic boutons on pyramidal cell

somata were PV+, 45% CB1R+ and only 0.5 % were double-negative (n=200 boutons in 2 mice), which numbers are in a very good agreement with previous data (Takács et al., 2015). For the electron tomographic examinations, we performed immunogold labeling against CB1R (Fig. 1. B). Once the mitochondrion-containing boutons from both populations were sampled, the presence of a synapse was confirmed for each bouton (Fig. 1. D, F). The sections containing the largest cross-sections of mitochondria were processed for dual-axis electron tomography and reconstruction, which revealed robust ultrastructural differences between these organelles, depending on which population they belonged to (Fig. 1. E, G, Fig S2.). Crista-membrane density (surface area of crista membrane/mitochondrial volume) was significantly higher (by 79.7%) in mitochondria of PV-boutons (median: 0.0408 nm^{-1}, interquartile range: 0.0389-0.0519) than in those from CB1R+ boutons (median: 0.0227 nm^{-1}, interquartile range: 0.0218-0.0256, Mann-Whitney U-test, p=0.0002, n=20 mitochondria from 2 mice, Fig. 1. H). When we multiplied these crista membrane density values with the median volume of presynaptic mitochondria ($119x10^6$ nm^3 in PV and 73.4 $x10^6$ nm^3 in CB+ boutons from Takács et al., 2015) we found a striking difference, showing that the average PV+ bouton utilizes 2.9 times more mitochondrial crista membrane surface than the average CB1+ bouton. The organisation of the cristae also differed, since these structures were significantly more lamellar in mitochondria of PV-boutons than in those from CB1R+ boutons, as verified by the 22%-higher crista shape factor values (surface area of crista membrane/crista lumen volume, PV median: 0.233 nm^{-1}, interquartile range: 0.218-0.251, CB1R median: 0.191 nm^{-1}, interquartile range: 0.147-0.220, Mann-Whitney U-test, p=0.0090, n=20 mitochondria from 2 mice, Fig. 1. I). These results suggest a strong correlation between the ultrastructure of presynaptic mitochondria and the performance of the synapses.

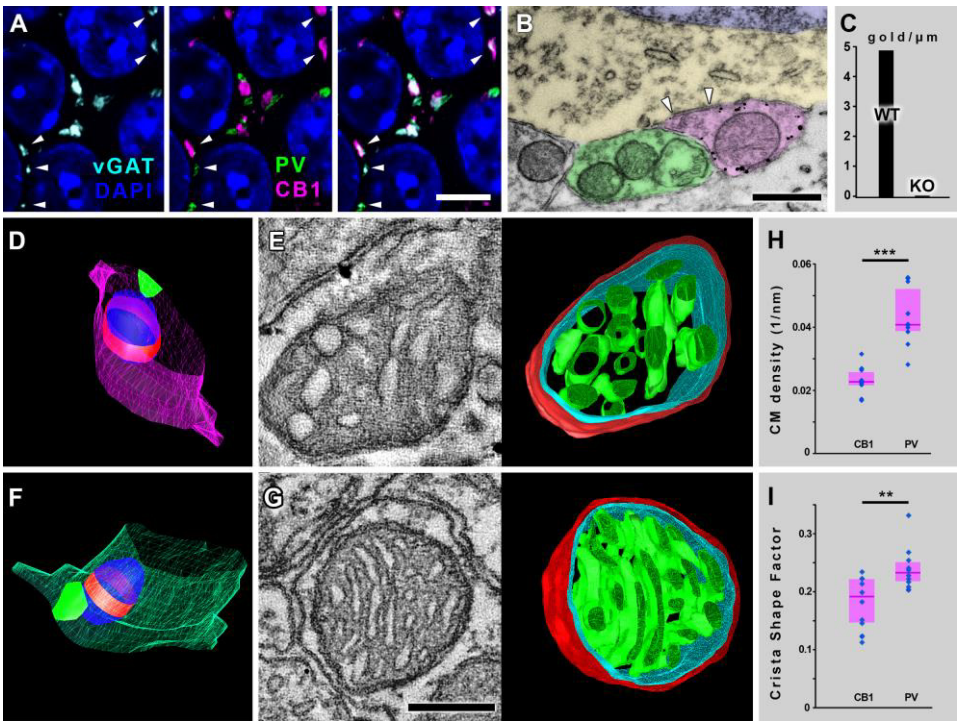

Fig. 1. Electron tomography reveals robust ultrastructural differences between axonal mitochondria of fast-spiking and regular-spiking basket cells. (A) Confocal images show that perisomatic synaptic boutons are either PV- or CB1R-positive in the hippocampal CA1 region. Pyramidal cell nuclei are labeled with DAPI (blue), vGAT-immunoreactive puncta represent GABAergic vesicle pools (cyan), PV-labeling is green and CB1R-labeling is magenta. (B) Transmission electron micrograph shows that CB1R-immunogold labeling reliably differentiates the two perisomatic bouton populations. Black granules are the silver-intensified CB1R-immunogold particles, white arrowheads mark a synapse. Pseudocolors: CB1R+ bouton – magenta, PV bouton – green, pyramidal cell cytoplasm – yellow and nucleus – blue. (C) CB1R-immunogold labeling was absent in CB1R-KO animals (tested membrane length: 38 µm in two WT, and 74.8 µm in two CB1R-KO mice). (D, F) Representative 3D-models of serial EM reconstructed segments from a synaptic CB1R+ bouton (D), and a synaptic PV bouton. Bouton membrane is magenta for CB1R-bouton, green for PV-bouton, synapses are vivid-green, mitochondria are blue, red belts represent those sections of the organelles that were reconstructed through electron tomography. (E) 1.5 nm thick electron tomographic section and 3D-model of the reconstructed mitochondrion from the bouton depicted in D (mitochondrial outer membrane is red, inner boundary membrane is cyan, crista membrane is green). (G) 1.5 nm thick electron tomographic section and 3D-model of the reconstructed mitochondrion from the bouton depicted in F. (H) Crista-membrane density is significantly higher in mitochondria of PV-boutons than in those from CB1R+ boutons (Mann-Whitney U-test, p=0.0002, n=20 mitochondria from 2 mice). (I) Cristae are significantly more lamellar in mitochondria of PV-boutons than in those from CB1R+ boutons, as verified by the higher crista shape factor values (Mann-Whitney U-test, p=0.0090, n=20 mitochondria from 2 mice). (H, I) Blue dots represent values from individual mitochondria, magenta rectangles represent interquartile ranges, deep-magenta lines mark median values. Scale bars are 6 µm in A, 500 nm in B and 100 nm in G and for E. The 3D models on E and G are not displayed on the same scale. See also Figures S1-S2.

STORM super-resolution microscopy confirms higher mitochondrial cytochrome-c density in boutons of fast-spiking basket cells than in regular-spiking ones

To assess whether the observed ultrastructural differences are accompanied by any changes in respiratory chain protein expression, we turned to a combined stochastic optical reconstruction microscopy (STORM) and confocal laser-scanning microscopy (CLSM) method, and performed precise quantitative assessment of cytochrome-c (CytC) levels in mitochondria. This protein is an indispensable element of the electron-transport chain, as it carries electrons to the cytochrome-c oxidase enzyme. CytC expression directly controls oxidative phosphorylation (Wilson et al., 2014), and its levels are indicative of mitochondrial performance and show good correlation with neuronal activity (Gulyás et al., 2006; Kann et al., 2014). To take advantage of the unprecedented 20-30 nm lateral localisation precision and qunatitative nature of the STORM super-resolution technique (Huang et al., 2008) and delineate mitochondrial borders with high fidelity, we performed double labeling experiments. If the distribution of CytC is homogenous within individual mitochondria, then the CytC super-resolution localisation point (SLP) clusters would designate the borders of these organelles in a reliable way. In this case, one could measure the sizes of these clusters and compare the SLP-density values between different mitochondria. To test this, we stained for TOM20 (central component of the translocase of outer membrane receptor complex) and CytC (Fig. 2. A). The measured sizes of individual mitochondria in the two STORM channels showed a very strong correlation (R=0.98, n=48 mitochondria from 2 mice, Fig. 2. B), excluding the non-homogenous sub-organelle distribution of CytC labeling. The median number of CytC SLPs labeling a single mitochondrion was 217 (interquartile range: 97-330). These results confirmed, that the CytC-labeling and STORM imaging can be used to delineate the borders of mitochondria in a precise and reliable way. Next, we performed a multi-color immunofluorescent labeling for PV, CB1R and CytC, and imaged the samples using correlated confocal and STORM super-resolution microscopy (Fig. 2. C-G). The CytC-labeling was recorded with the STORM system as well. The STORM SLP-s were overlayed the confocal images with the VividSTORM software (Fig. 2. D, F). The analysis showed, that mitochondria in the PV+ boutons were larger than those in the CB1R+ boutons, as the 2D areas of the convex hulls – fitted around SLP-clusters – were 75.4% larger in the former group (median: 0.287 μm^2, interquartile range: 0.158-0.368) than in the latter (median: 0.164 μm^2, interquartile range: 0.098-0.203, Mann-Whitney U-test, p=0.0085, n=57 mitochondria from 2 mice, Fig. 2. H). More importantly we found, that mitochondria in the PV+ boutons contained CytC SLPs in a 22.7% higher density (median: 565.7 SLP/μm^2, interquartile range:

434.8-725.7) than those in the CB1R+ boutons (median: 461.1 SLP/µm^2, interquartile range: 378.8-612.0, Mann-Whitney U-test, p=0.0384, n=57 mitochondria from 2 mice, Fig. 2. I). These results confirm that the internal structural differences between the mitochondria in the two bouton populations are accompanied by quantitative differences in molecular fingerprints as reflected by the levels of the respiratory chain protein cytochrome-c.

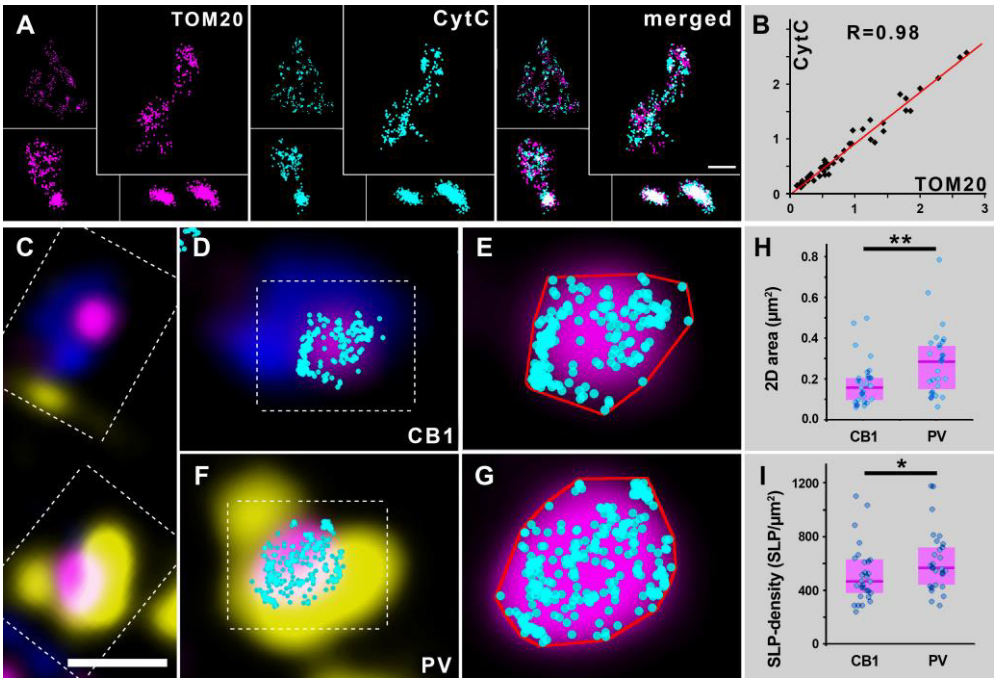

Fig. 2. Axonal mitochondria of fast-spiking basket cells express higher levels of cytochrome-c than those of regular-spiking basket cells'. (A) STORM super-resolution imaging confirms a near-complete overlap between TOM20 and cytochrome-c labeling. (B) Scatterplot shows a strong correlation (R=0.98, n=48 mitochondria from 2 mice) between the measured areas in the two channels of individual mitochondria. Each dot corresponds to a single mitochondrion. (C) Confocal image shows a CB1R+ (blue) and a PV+ (yellow) perisomatic bouton, both containing a mitochondrion, labeled for cytochrome-c (magenta). (D) CB1R+ bouton enlarged from C with overlaid STORM cytochrome-c localisation points (cyan). (E) Confocal and STORM image of mitochondrion enlarged from D. (F) PV+ bouton enlarged from C with overlaid STORM cytochrome-c localisation points. (G) Confocal and STORM image of mitochondrion enlarged from D. Red lines in E and G mark the 2D convex hulls generated around the localisation points. (H) Mitochondria in the PV+ boutons are larger than those in the CB1R+ boutons, as the 2D areas of the convex hulls are significantly larger in the former group (Mann-Whitney U-test, p=0.0085, n=57 mitochondria from 2 mice). (I) Mitochondria in the PV+ boutons contain cytochrome-c in a higher density than those in the CB1R+ boutons (Mann-Whitney U-test, p=0.0384, n=57 mitochondria from 2 mice). Blue dots represent values from individual mitochondria, magenta rectangles represent interquartile ranges, deep-magenta lines mark median values. Scale bar in A is 800 nm for upper-left mitochondrion, 400 for all others; scale bar in C is 1 µm, 600 nm for D and F and 170 nm for E and G.

Ultrastructural parameters of presynaptic mitochondria in glutamatergic boutons are coupled to synaptic strength

To confirm that the observed correlations between molecular and structural mitochondrial properties and synaptic features are independent of the cell types examined, we investigated glutamatergic synaptic boutons in the dentate gyrus. One of the best characterized structure-function correlations in neuroscience is that synaptic strength is strictly and faithfully linked to morphological/ultrastructural parameters (Bourne and Harris, 2012; Buchs and Muller, 1996; Cheetham et al., 2014; Desmond and Levy, 1988; Holtmaat and Svoboda, 2009). The release probability of these synapses scales linearly with the size of the active zone (Holderith et al., 2012), and long-term potentiation leads to an increase in the size of synaptic active zone, the number of perforated synapses and also in the number of boutons with multiple active zones (Geinisman, 2000; Popov et al., 2004). Based on this fundamental morpho-functional correlation, the strength of glutamatergic synapses can be determined purely by morphological critera in a very reliable way, enabling us to define a "low performance" and a "high performance" group within a specific glutamatergic synaptic boutons population. We randomly collected samples from the outer two-thirds of the dentate gyrus molecular layer, where the vast majority of all glutamatergic contacts are made by perforant path axons (Amaral et al., 2007), and reconstructed synaptic boutons from serial EM sections together with the postsynaptic neuronal processes (Fig. 3. A, C). The median active zone area was found to be 0.070 μm^2 (0.042-0.123 μm^2 interquartile range, n=35 synaptic boutons in 2 mice, Fig. S4. A). About half of these boutons contained mitochondria, and the active zone area in this group did not differ significantly from the previous group, as it was found to be 0.093 μm^2 (0.048-0.171 μm^2 interquartile range, Mann-Whitney U-test, p=0.267; n=19 synaptic boutons in 2 mice, Fig. S4. A). Based on these data and the strict correlation between synaptic ultrastructure and performance, we grouped the reconstructed mitochondria-containing varicosities as follows: boutons were considered to be "low performance" (LP), if they had a single, non-perforated active zone with an area less than 0.09 μm^2, and boutons were considered to be „high performance" (HP), if they had multiple and/or peforated active zone(s) with an area larger than 0.09 μm^2 (Fig. S4. A). We measured the mitochondrial volumes in the 3D-models, and found that presynaptic mitochondria in HP-boutons were significantly larger than those in LP-boutons (HP-median: 41.8×10^6 nm^3, 25×10^6-46.5×10^6 interquartile range, LP-median: 18.9×10^6 nm^3, 13×10^6-27.6×10^6 interquartile range, 121.6% difference, Mann-Whitney U-test, p=0.0199, n=19 boutons from two mice; Fig. 3. E). The sections containing the largest cross-sections of presynaptic mitochondria of these boutons

were processed for dual-axis electron tomography and reconstruction, which revealed robust ultrastructural differences between these organelles, depending on which population they belonged to (Fig. 3. B, D, Fig. S3.). Crista-membrane density (surface area of crista membrane/mitochondrial volume) was significantly higher (by 110.1%) in mitochondria of HP-boutons (median: 0.0552 nm^{-1}, interquartile range: 0.0509-0.0587) than in those from LP-boutons (median: 0.0262 nm^{-1}, interquartile range: 0.0258-0.0290, Mann-Whitney U-test, p=0.0009, n=19 mitochondria from 2 mice, Fig. 3. F). We then multiplied these crista membrane density values with the median volume of presynaptic mitochondria ($41.8x10^6$ nm^3 in HP and $18.9x10^6$ nm^3 in LP boutons), and found a striking difference, showing that the average HP bouton utilizes 4.67 times more mitochondrial crista membrane surface than the average LP bouton. The organisation of the cristae also differed significantly, since these structures were more lamellar in mitochondria of HP-boutons than in those from LP-boutons, as verified by the 37.8% higher crista shape factor values (surface area of crista membrane/crista lumen volume) in the former group (median: 0.268, interquartile range: 0.237-0.301), than in the latter (median: 0.195, interquartile range: 0.190-0.219, Mann-Whitney U-test, p=0.0080, n=19 mitochondria from 2 mice, Fig. 3. G). To verify the robustness of our results, we pooled data from HP and LP boutons, and examined whether the different ultrastructural features correlated with the size of the synaptic active zone. We found that the volume, crista-membrane density and crista shape factor of presynaptic mitochondria are all strongly and significantly correlated with synapse size, (R=0.71, p=0.0005; R=0.77, p=0.0001; and R=0.65, p=0.0026, respectively; Pearson correlation, n=19 mitochondria from 2 mice, Fig. S4. B). We also tested our findings on post-mortem human tissue. We collected a random sample of mitochondria-containing presynaptic axon segments, reconstructed them from serial sections (Fig. 3. H), and found a strong and significant correlation between the active zone area and the volume of individual presynaptic mitochondria (R=0.78, p=0.0003, Pearson correlation, n=16 mitochondria from one patient, Fig. 3. I, J), confirming the results from mouse studies. In summary, our results reveal for the first time that the ultrastructure of presynaptic mitochondria is predictive of synaptic performance in the brain, in a cell-type independent manner.

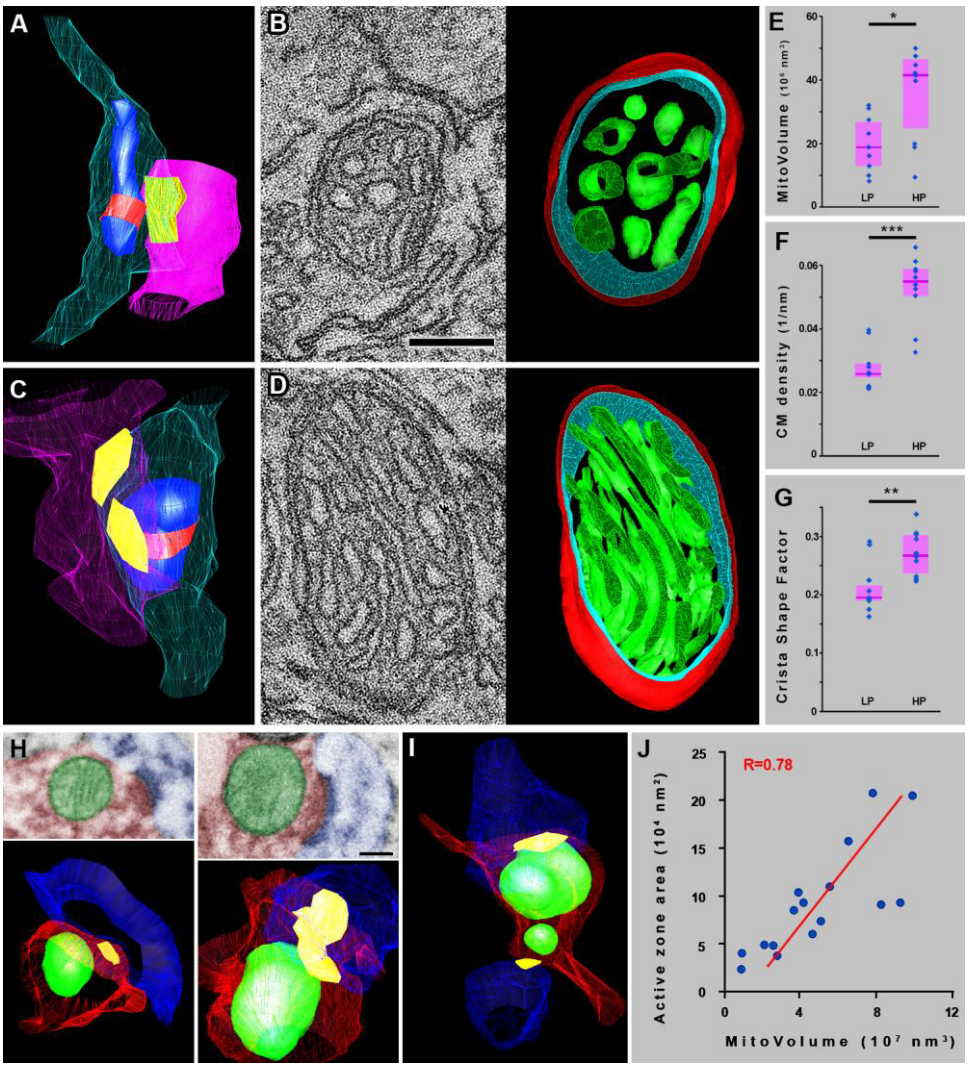

Fig. 3. Mitochondrial ultrastructure is coupled to synaptic performance in a cell-type independent manner at glutamatergic synapses. (A) 3D-model of a serial EM reconstructed segment of a „low performance" glutamatergic bouton from the dentate-gyrus. Bouton membranes are semi-transparent cyan, postsynaptic profiles are semi-transparent magenta, synapse are yellow, mitochondria are blue, red belts mark those sections of the organelles that were reconstructed through electron tomography. (B) 1.5 nm thick electron tomographic section and 3D-model of the reconstructed mitochondrion from the bouton depicted in A (mitochondrial outer membrane is red, inner boundary membrane is cyan, crista membrane is green). (C) 3D-model of a serial EM reconstructed segment of a „high performance" glutamatergic bouton from the dentate-gyrus (colors same as in A). (D) 1.5 nm thick electron tomographic section and 3D-model of the reconstructed mitochondrion from the bouton depicted in C. (E) Mitochondria are significantly larger in „high performance"-boutons than in „low performance"-boutons (Mann-Whitney U-test, p=0.0199, n=19 mitochondria from 2 mice). (F) Crista-membrane density is significantly higher in mitochondria of „high performance"-boutons than in those from „low performance"-boutons (Mann-Whitney U-test, p=0.0009, n=19 mitochondria from 2 mice). (G) Cristae are significantly more lamellar in mitochondria of „high performance"-boutons than in those from „low performance"-boutons, as verified by the higher crista shape factor values (Mann-Whitney U-test, p=0.0080, n=19 mitochondria from 2 mice). (H-J) The volume of individual presynaptic mitochondria correlates with active zone area in the human hippocampus. (H) Transmission electron micrographs of two presynaptic

mitochondria from human samples, and their 3D-reconstructions from serial images. (I) 3D-model of an axonal segment from human tissue, giving two synapses, each with an associated presynaptic mitochondrion. Axons are red, mitochondria green, spines blue and active zones yellow. (J) The volume of presynaptic mitochondria shows a strong correlation with active zone area in human axons (R=0.78, p=0.0003). (E-G, J) Blue dots represent values from individual mitochondria, magenta rectangles represent interquartile ranges, deep-magenta lines mark median values. Scale bar is 110 nm in B and for D, 200 nm on H. The 3D models on B, D and H are not displayed on the same scale. See also Figures S3-S4.

Cytochrome-c density in presynaptic mitochondria of glutamatergic boutons scales with synaptic strength

To examine whether the observed cell-type independent coupling between mitochondrial ultrastructure and synaptic performance is accompanied also by changes in respiratory chain protein expression levels, we tested the density of CytC-labeling in mitochondria of „low-performance" (LP) and „high-performance" (HP) glutamatergic synaptic boutons, using correlated confocal and STORM super-resolution microscopy, taking advantage of the near-molecular resolution capability of this method. We labeled glutamategic boutons against vesicular glutamate transporter 1 (VG1), mitochondria with CytC, and postsynaptic densities with Homer1 (Fig. 4. A, C). We sampled mitochondria-containing synaptic boutons from the outer two-thirds of DG molecular layer, and reconstructed them from the deconvolved confocal stacks (Fig. 4. B, D). The volumes of Homer labeling belonging to each bouton were measured on the 3D models, and the median value was found to be 0.0265 μm^3 (0.011-0.0518 interquartile range, Fig. S4. C). These values correspond to the size of the active zone in each bouton, meaning that this distribution indirectly reflects the output performance distribution of the examined boutons. Based on these data, we split the population at the median value, and sorted boutons with a lower Homer volume into the LP-group, and boutons with higher values into the HP-group (Fig. S4. C). We found that presynaptic mitochondria in HP-boutons were significantly larger than those in LP-boutons (HP-median: 0.0365 μm^3, 0.0282-0.0578 interquartile range, LP-median: 0.0162 μm^3, 0.0150-0.0265 interquartile range, 128.8% difference, Mann-Whitney U-test, p=0.0003, n=42 boutons from two mice; Fig. 4. G), and this observed difference is congruent with our serial EM data (128.8% vs. 121.6% difference). The CytC-labeling was recorded not only in the confocal channel, but also in the correlated STORM modality. The STORM SLP-s were overlayed the confocal images (Fig. 4. C, F). We found that the CytC SLP density was 61% higher in mitochondria of HP-boutons than in those of LP-boutons (HP-median: 598.5

SLP/ µm^2, 455.6-822 interquartile range, LP-median: 370.8, 296.3-440.7 interquartile range, Mann-Whitney U-test, p=0.0001, n=42 boutons from two mice; Fig. 4. H). To verify the strength of our results, we pooled data from HP and LP boutons, and examined whether the investigated features correlated with the size of the synaptic active zone. We found, that the CytC-labeled volume and SLP-density are both strongly correlated to synapse size, (R=0.77, p<0.00001; R=0.60, p=0.00002, respectively; Spearman's correlation, n=42 mitochondria from 2 mice, Fig. S4. D). Taken all these together, our results confirm that not only the mitochondrial nano-architecture is coupled to synaptic performance in a cell-type independent manner, but also the expression levels of the respiratory chain protein cytochrome-c.

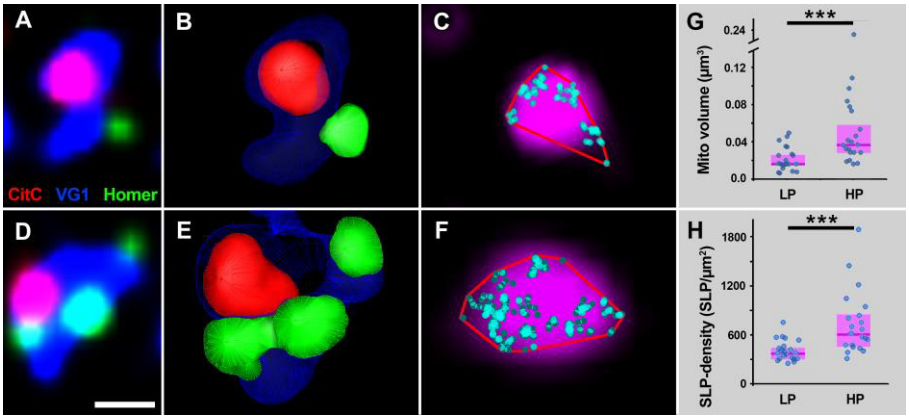

Fig. 4. Cytochrome-c content of presynaptic mitochondria scales with synaptic performance at glutamatergic synapses (A) Confocal image shows a glutamatergic bouton (VG1, blue), containing a mitochondrion (Cyt-C, red), and its synapse (Homer1a, green). (B) The 3D-model of the bouton from A was reconstructed from the confocal stack. (C) Confocal and STORM image of mitochondrion enlarged from the same bouton (Cyt-C confocal in magenta, Cyt-C localisation points in cyan, 2D convex hull in red). (D-F) Another bouton depicted as in A-C. Mitochondria-containing synaptic boutons were divided into „low-performance" (LP) and „high-performance" (HP) groups, based on the corresponding Homer volumes. Bouton in A-C represents a LP, bouton in D-F represents a HP bouton. (G) Mitochondria in the HP-boutons are larger than those in the LP-boutons, as the CytC-volumes are significantly larger in the former group (Mann-Whitney U-test, p=0.00032, n=42 mitochondria from 2 mice). (H) Mitochondria in the HP-boutons contain cytochrome-c in a higher density than those in the HP-boutons (Mann-Whitney U-test, p=0.00016, n=42 mitochondria from 2 mice). Blue dots represent values from individual mitochondria, magenta rectangles represent interquartile ranges, deep-magenta lines mark median values. Scale bar is 800 nm for A and D, and 200 nm for C and F. The 3D models on B and E are not displayed on the same scale. See also Figure S4.

DISCUSSION

Mitochondrial and synaptic performance are coupled via sub-organelle ultrastructure

The first observations suggesting a connection between mitochondrial crista-structure and function were obtained on *ex vivo* isolated mitochondria (Hackenbrock, 1966). Although those specific results have not been verified under physiological conditions, causal correlation between mitochondrial ultrastructure and output performance in non-neuronal cells has been confirmed in recent studies (Cogliati et al., 2016). The amount and density of cristae membrane as well as the tightness of cristae directly determine respiratory performance and efficiency (Cogliati et al., 2013; Else et al., 2004), and these ultrastructural features were also shown to influence performance at the level of the complete organism (Strohm and Daniels, 2003). On the other hand, aberrant morphology, dilatation or loss of mitochondrial cristae have been observed in a variety of pathological conditions (Choi et al., 2014; Daum et al., 2013), while genetic manipulations ameliorating damaged crista-structure have been shown to restore normal crista density/tightness and respiratory chain activity (Civiletto et al., 2015). Furthermore, modelling studies also confirmed, that crista-membrane density and tightness are key determinants of mitochondrial electrochemical potential and ATP-generating capacity (Song et al., 2013). There are several points explaining the correlation between mitochondrial ultrastructure and performance: larger crista-membrane surface can accomodate a higher amount of respiratory chain and ATP-synthase proteins, leading to a higher respiratory and ATP-generating capacity, whilst tighter cristae structure is beneficial for respiratory chain supercomplex assembly, resulting in a higher respiratory efficiency. Furthermore, tighter cristae – independently from changes in respiratory efficacy – result in an increased proton motive force, leading to higher ATP-producing capacity. Finally, ATP-synthase molecules tend to be enriched and dimerize at curved cristae-rims, making the dense and tight packing of these membranes more effective to produce ATP (Davies et al., 2011).

Mitochondria are critically important for proper synaptic function, due to their central role in ATP-production, Ca^{2+}-regulation and other major signalling mechanisms. In particular, presynaptic function has been shown to rely directly on activity-driven ATP synthesis (Rangaraju et al., 2014). The demand for mitochondrial function is reasonably coupled to neuronal activity (Gulyás et al., 2006; Kann et al., 2014) and also directly correlated with synaptic strength (Ivannikov et al., 2013; Smith et al., 2016; Sun et al., 2013; Verstreken et al., 2005). Our results demonstrate that increased synaptic performance is coupled to higher organelle volume, crista density, crista tightness and cytochrome-c levels at axonal release

sites, suggesting that fine-architecture and molecular composition of the mitochondria are associated with synaptic performance.

Performance coupling between mitochondria and synapses suggest a role for the activity dependent ultrastructural remodelling of mitochondria in neuroplasticity

Mitochondrial inner membrane architecture has been shown to undergo substantial remodelling after exercise, under hypoxic conditions or during starvation (Gomes et al., 2011; Hambrecht et al., 1997; Nielsen et al., 2016; Perkins et al., 2012), suggesting that the local demand for mitochondrial performance is communicated to these organelles, prompting their activity-dependent ultrastructural plasticity. The common response to an increased energetic demand was an increased crista-membrane density and tightness in all of these cases. The idea of mitochondrial ultrastructural adaptation is also supported by a study, confirming that crista remodelling can happen on the timescale of minutes (Dikov and Bereiter-Hahn, 2013). In recent years, various mechanisms have been described to regulate mitochondrial ultrastructure, such as mitochondrial dynamin like GTPase (OPA1), mitochondrial contact site and cristae organizing system (MICOS), ATP-synthase dimerisation and the inner-membrane protein Pantagruelian Mitochondrion I (Gomes et al., 2011; Hahn et al., 2016; Harner et al., 2011; Macchi et al., 2013; Neupert, 2012). Substrate dependent changes in OPA1 expression levels (Patten et al., 2014; Sood et al., 2014), or activity-dependent ATP-synthase clustering (Jimenez et al., 2014) are known to contribute to mitochondrial ultrastructural plasticity.

Synaptic mitochondria possess a specific proteome (Völgyi et al., 2015), and local axonal protein synthesis has also been shown to be required for the maintenance of mitochondrial function (Aschrafi et al., 2008; Gale et al., 2017; Hillefors et al., 2007). Thus, it is very likely that local presynaptic signalling mechanisms regulate the expression of mitochondrial proteins in axons, thereby controlling mitochondrial ultrastructure and performance. On the other hand, recently it was also described that – unlike *in vitro* – axonal mitochondrial motility is rather limited *in vivo*, and fairly independent from synaptic activity (Lewis et al., 2016; Smit-Rigter et al., 2016). All these findings – together with our results – suggest that the primary way of adjusting mitochondrial performance to the actual demand at synapses could be the activity-dependent ultrastructural plasticity of these organelles. Furthermore, our results – confirming a cell-type independent coupling between synaptic performance and mitochondrial ultrastructure – indicate that these changes in mitochondrial nano-architecture and molecular fingerprints could contribute to neuroplasticity at the level of individual synapses.

EXPERIMENTAL PROCEDURES

Refer to Supplemental Experimental Procedures for detailed methods.

Animals, tissue preparation and immunolabeling

All experimental procedures were in accordance with the guidelines set by the European Communities Council Directive (86/609 EEC) and the Hungarian Act of Animal Care and Experimentation (1998; XXVIII, section 243/1998), approved by the Animal Care and Use Committee of the IEM HAS. Mice were perfused transcardially with aldehyde fixatives, and 20, 50 or 60 µm thick coronal sections were cut on a vibratome for STORM, CLSM and EM experiments, respectively. Incubation of sections with primary and secondary antibodies was performed in free-floating manner for all experiments. After staining, sections were dried onto coverslips for STORM imaging, coverslipped onto glass slides with Aquamount for CLSM, dehydrated and embedded in epoxy resin for EM. We used control human hippocampal tissue from a female subject (59 years old) who had no history of brain disorders. All procedures were approved by the Regional and Institutional Committee of Science and Research Ethics of Scientific Council of Health (Medical Research Council National Scientific and Ethical Committee [ETT TUKEB] 31443/2011/EKU [518/PI/11]).

Confocal laser-scanning microscopy and STORM super-resolution microscopy

Immunofluorescence was analyzed using a Nikon Eclipse Ti-E inverted microscope, an A1R laser confocal system and NIS-Elements AR software. Correlated CLSM-STORM imaging was performed with a Nikon Ti-E inverted microscope, a C2 confocal head, an Andor iXon Ultra 897 EMCCD camera and the NIS-Elements AR 4.3 with N-STORM 3.4 software.

Immunoelectron-microscopy and electron-tomography

After dehydration, resin-embedded tissue samples were glued to blocks, and ultrathin sections were cut on a Leica UC6 ultramicrotome. Before electron tomography, 100-200 nm thick serial sections on single-slot copper grids were photographed with a Hitachi H-7100 electron microscope and a Veleta CCD camera. 10 nm gold particles were applied for fiducial markers, then 5-5 nm thick layers of carbon were deposited on both sides of the grids. Electron tomography was performed using a Tecnai T12 BioTwin electron microscope controlled via the Xplore3D software (FEI). Dual-axis tilt series were collected at 2 degree

increment steps between -65 and +65 degrees at 120 kV acceleration voltage and 23000x magnification with -1.6 – -2 µm objective lens defocus. Reconstruction was performed using the IMOD software package (Kremer at al., 1996).

Analysis and statistics

CLSM data was analysed with Nikon Elements AR and Fiji softwares, STORM analysis was performed using the VividSTORM open source software (Barna et al, 2015). Tomographic analysis and 3D modeling was done with the IMOD package. When data populations did not have a Gaussian distribution according to the Shapiro-Wilks W test, we reported non-parametric statistical features (median, interquartile range), compared two independent groups with the Mann-Whitney U-test, and Spearman correlation coefficients were calculated. When data populations showed normal distribution, correlations were assessed using linear regression fit to the data (R indicates Pearson's correlation coefficient). Statistical analysis was performed with the Statistica 13.1 package (Dell), differences with $p<0.05$ were considered significant throughout this study.

SUPPLEMENTAL INFORMATION

Supplemental Information includes Supplemental Results, Supplemental Experimental Procedures and four figures and can be found online with the article.

AUTHOR CONTRIBUTIONS

Methodology C.C.; Investigation C.C. B. P. and A.S.; Conceptualization and Writing – Original Draft, C.C.; Writing – Review & Editing, C.C. and A.D.; Funding Acquisition, A.D.; Resources, C.C. and A.D.; Supervision, C.C. and A.D.

ACKNOWLEDGEMENTS

This work was supported by „Momentum" research grant from the Hungarian Academy of Sciences (LP2016-4/2016 to A.D.) and ERC-CoG 724994 (A.D.). We thank László Barna and the Nikon Imaging Center at the Institute of Experimental Medicine for kindly providing microscopy support, and David Mastronarde at MCDB for his continous help with IMOD software. We thank the Department of Pathology, St. Borbála Hospital, Tatabánya, and the Human Brain Research Lab at the Institute of Experimental Medicine, Hungarian Academy of Sciences (IEM HAS) for providing human

brain tissue. We also thank Dr. Gábor Nyiri, Prof. Ken Mackie and Prof. Andreas Zimmer for the CB1R antibodies and CB1R-KO animals; and Dóra Gali-Györkei for her excellent technical assistance.

REFERENCES

Amaral, D.G., Scharfman, H.E., and Lavenex, P. (2007). The dentate gyrus: fundamental neuroanatomical organization (dentate gyrus for dummies). Prog. Brain Res.

Aschrafi, A., Schwechter, A.D., Mameza, M.G., Natera-Naranjo, O., Gioio, A.E., and Kaplan, B.B. (2008). MicroRNA-338 regulates local cytochrome c oxidase IV mRNA levels and oxidative phosphorylation in the axons of sympathetic neurons. J. Neurosci. *28*, 12581–12590.

Barnhart, E.L. (2016). Mechanics of mitochondrial motility in neurons. Curr. Opin. Cell Biol.

Billups, B., and Forsythe, I.D. (2002). Presynaptic mitochondrial calcium sequestration influences transmission at mammalian central synapses. J. Neurosci. *22*, 5840–5847.

Bourne, J.N., and Harris, K.M. (2012). Nanoscale analysis of structural synaptic plasticity. Curr. Opin. Neurobiol. *22*, 372–382.

Buchs, P.A., and Muller, D. (1996). Induction of long-term potentiation is associated with major ultrastructural changes of activated synapses. Proc. Natl. Acad. Sci. U. S. A. *93*, 8040–8045.

Chandel, N.S. (2014). Mitochondria as signaling organelles. BMC Biol. *12*.

Cheetham, C.E.J., Barnes, S.J., Albieri, G., Knott, G.W., and Finnerty, G.T. (2014). Pansynaptic enlargement at adult cortical connections strengthened by experience. Cereb. Cortex *24*, 521–531.

Choi, K.J., Kim, M.J., Je, A.R., Jun, S., Lee, C., Lee, E., Jo, M., Huh, Y.H., and Kweon, H.S. (2014). Three-dimensional analysis of abnormal ultrastructural alteration in mitochondria of hippocampus of APP/PSEN1 transgenic mouse. J. Biosci.

Civiletto, G., Varanita, T., Cerutti, R., Gorletta, T., Barbaro, S., Marchet, S., Lamperti, C., Viscomi, C., Scorrano, L., and Zeviani, M. (2015). Opa1 overexpression ameliorates the phenotype of two mitochondrial disease mouse models. Cell Metab.

Cogliati, S., Frezza, C., Soriano, M.E., Varanita, T., Quintana-Cabrera, R., Corrado, M., Cipolat, S., Costa, V., Casarin, A., Gomes, L.C., et al. (2013). Mitochondrial cristae shape determines respiratory chain supercomplexes assembly and respiratory efficiency. Cell.

Cogliati, S., Enriquez, J.A., and Scorrano, L. (2016). Mitochondrial Cristae: Where Beauty Meets Functionality. Trends Biochem. Sci.

Daum, B., Walter, A., Horst, A., Osiewacz, H.D., and Kühlbrandt, W. (2013). Age-dependent dissociation of ATP synthase dimers and loss of inner-membrane cristae in mitochondria. Proc. Natl. Acad. Sci. U. S. A. *110*, 15301–15306.

Davies, K.M., Strauss, M., Daum, B., Kief, J.H., Osiewacz, H.D., Rycovska, A., Zickermann, V., and Kuhlbrandt, W. (2011). Macromolecular organization of ATP synthase and complex I in whole mitochondria. Proc. Natl. Acad. Sci. *108*, 14121–14126.

Desmond, N.L., and Levy, W.B. (1988). Synaptic interface surface area increases with long-term potentiation in the hippocampal dentate gyrus. Brain Res *453*, 308–314.

Dikov, D., and Bereiter-Hahn, J. (2013). Inner membrane dynamics in mitochondria. J. Struct. Biol.

Else, P.L., Turner, N., and Hulbert, A.J. (2004). The evolution of endothermy: role for membranes and molecular activity. Physiol. Biochem. Zool. *77*, 950–958.

Gale, J.R., Aschrafi, A., Gioio, A.E., and Kaplan, B.B. (2017). Nuclear-Encoded Mitochondrial mRNAs: A Powerful Force in Axonal Growth and Development. Neurosci. 107385841771422.

Gazit, N., Vertkin, I., Shapira, I., Helm, M., Slomowitz, E., Sheiba, M., Mor, Y., Rizzoli, S., and Slutsky, I. (2016). IGF-1 Receptor Differentially Regulates Spontaneous and Evoked Transmission via Mitochondria at Hippocampal Synapses. Neuron.

Geinisman, Y. (2000). Structural synaptic modifications associated with hippocampal LTP and behavioral learning. Cereb. Cortex *10*, 952–962.

Gomes, L.C., Di Benedetto, G., and Scorrano, L. (2011). During autophagy mitochondria elongate, are spared from degradation and sustain cell viability. Nat. Publ. Gr. *13*.

Gulyás, A.I., Buzsáki, G., Freund, T.F., and Hirase, H. (2006). Populations of hippocampal inhibitory neurons express different levels of cytochrome c. Eur. J. Neurosci.

Gunter, T.E., Buntinas, L., Sparagna, G., Eliseev, R., and Gunter, K. (2000). Mitochondrial calcium transport: mechanisms and functions. Cell Calcium *28*, 285–296.

Hackenbrock, C.R. (1966). Ultrastructural bases for metabolically linked mechanical activity in mitochondria. I. Reversible ultrastructural changes with change in metabolic steady state in isolated liver mitochondria. J. Cell Biol. *30*, 269–297.

Hahn, A., Parey, K., Bublitz, M., Mills, D.J., Zickermann, V., Vonck, J., K??hlbrandt, W., and Meier, T. (2016). Structure of a Complete ATP Synthase Dimer Reveals the Molecular Basis of Inner Mitochondrial Membrane Morphology. Mol. Cell.

Hall, C.N., Klein-Flugge, M.C., Howarth, C., and Attwell, D. (2012). Oxidative Phosphorylation, Not Glycolysis, Powers Presynaptic and Postsynaptic Mechanisms Underlying Brain Information

Processing. J. Neurosci. *32*, 8940–8951.

Hambrecht, R., Fiehn, E., Yu, J., Niebauer, J., Weigl, C., Hilbrich, L., Adams, V., Riede, U., and Schuler, G. (1997). Effects of endurance training on mitochondrial ultrastructure and fiber type distribution in skeletal muscle of patients with stable chronic heart failure. J. Am. Coll. Cardiol. *29*, 1067–1073.

Harner, M., Körner, C., Walther, D., Mokranjac, D., Kaesmacher, J., Welsch, U., Griffith, J., Mann, M., Reggiori, F., and Neupert, W. (2011). The mitochondrial contact site complex, a determinant of mitochondrial architecture. EMBO J. *30*, 4356–4370.

Harris, J.J., Jolivet, R., and Attwell, D. (2012). Synaptic Energy Use and Supply. Neuron.

Hillefors, M., Gioio, A.E., Mameza, M.G., and Kaplan, B.B. (2007). Axon viability and mitochondrial function are dependent on local protein synthesis in sympathetic neurons. Cell. Mol. Neurobiol.

Holderith, N., Lorincz, A., Katona, G., Kulik, A., Watanabe, M., and Nusser, Z. (2012). Release probability of hippocampal glutamatergic terminals scales with the size of the active zone. Nat. Neurosci.

Holtmaat, A., and Svoboda, K. (2009). Experience-dependent structural synaptic plasticity in the mammalian brain. Nat. Rev. Neurosci. *10*, 759–759.

Huang, B., Jones, S.A., Brandenburg, B., and Zhuang, X. (2008). Whole-cell 3D STORM reveals interactions between cellular structures with nanometer-scale resolution. Nat. Methods *5*, 1047–1052.

Ivannikov, M. V., Sugimori, M., and Llinás, R.R. (2013). Synaptic vesicle exocytosis in hippocampal synaptosomes correlates directly with total mitochondrial volume. J. Mol. Neurosci.

Jimenez, L., Laporte, D., Duvezin-Caubet, S., Courtout, F., and Sagot, I. (2014). Mitochondrial ATP synthases cluster as discrete domains that reorganize with the cellular demand for oxidative phosphorylation. J. Cell Sci. *127*, 719–726.

Kann, O., Papageorgiou, I.E., and Draguhn, A. (2014). Highly energized inhibitory interneurons are a central element for information processing in cortical networks. J. Cereb. Blood Flow Metab. *34*, 1270–1282.

Klausberger, T., Marton, L.F., O'Neill, J., Huck, J.H.J., Dalezios, Y., Fuentealba, P., Suen, W.Y., Papp, E., Kaneko, T., Watanabe, M., et al. (2005). Complementary roles of cholecystokinin- and parvalbumin-expressing GABAergic neurons in hippocampal network oscillations. J. Neurosci.

Lapray, D., Lasztoczi, B., Lagler, M., James Viney, T., Katona, L., Valenti, O., Hartwich, K., Borhegyi, Z., Somogyi, P., and Klausberger, T. (2012). Behavior-dependent specialization of identified hippocampal interneurons. Nat. Neurosci. *15*.

Lewis, T.L., Turi, G.F., Kwon, S.K., Losonczy, A., and Polleux, F. (2016). Progressive Decrease of Mitochondrial Motility during Maturation of Cortical Axons In Vitro and In Vivo. Curr. Biol.

Li, Z., Okamoto, K.I., Hayashi, Y., and Sheng, M. (2004). The importance of dendritic mitochondria in the morphogenesis and plasticity of spines and synapses. Cell.

Macchi, M., El Fissi, N., Tufi, R., Bentobji, M., Liévens, J.-C., Martins, L.M., Royet, J., and Rival, T. (2013). The Drosophila inner-membrane protein PMI controls crista biogenesis and mitochondrial diameter. J. Cell Sci. *126*, 814–824.

Mannella, C.A., Lederer, W.J., and Jafri, M.S. (2013). The connection between inner membrane topology and mitochondrial function. J Mol Cell Cardiol *62C*, 51–57.

Muller, D., Nikonenko, I., Jourdain, P., and Alberi, S. (2002). LTP, memory and structural plasticity. Curr. Mol. Med. *2*, 605–611.

Neupert, W. (2012). SnapShot: Mitochondrial Architecture. Cell *149*, 722–722.e1.

Nielsen, J., Gejl, K.D., Hey-mogensen, M., Holmberg, H.-C., Suetta, C., Krustrup, P., Elemans, C.P.H., and Ørtenblad, N. (2016). Plasticity in mitochondrial cristae density allows metabolic capacity modulation in human skeletal muscle Corresponding author : Key points. J. Physiol. 1–29.

Patten, D.A., Wong, J., Khacho, M., Soubannier, V., Mailloux, R.J., Pilon-larose, K., Maclaurin, J.G., Park, D.S., Mcbride, H.M., Trinkle-mulcahy, L., et al. (2014). OPA 1 -dependent cristae modulation is essential for cellular adaptation to metabolic demand. *33*, 2676–2691.

Perkins, G., Hsiao, Y. hsin, Yin, S., Tjong, J., Tran, M.T., Lau, J., Xue, J., Liu, S., Ellisman, M.H., and Zhou, D. (2012). Ultrastructural Modifications in the Mitochondria of Hypoxia-Adapted Drosophila melanogaster. PLoS One.

Perkins, G. a, Ellisman, M.H., and Fox, D. a (2003). Three-dimensional analysis of mouse rod and cone mitochondrial cristae architecture: bioenergetic and functional implications. Mol. Vis. *9*, 60–73.

Popov, V.I., Davies, H.A., Rogachevsky, V. V., Patrushev, I. V., Errington, M.L., Gabbott, P.L.A., Bliss, T.V.P., and Stewart, M.G. (2004). Remodelling of synaptic morphology but unchanged synaptic density during late phase long-term potentiation (LTP): A serial section electron micrograph study in the dentate gyrus in the anaesthetised rat. Neuroscience.

Rangaraju, V., Calloway, N., and Ryan, T.A. (2014). Activity-driven local ATP synthesis is required for synaptic function. Cell *156*, 825–835.

Sheng, Z.H. (2014). Mitochondrial trafficking and anchoring in neurons: New insight and implications. J. Cell Biol. *204*, 1087–1098.

Smit-Rigter, L., Rajendran, R., Silva, C.A.P., Spierenburg, L., Groeneweg, F., Ruimschotel, E.M., van

Versendaal, D., van der Togt, C., Eysel, U.T., Heimel, J.A., et al. (2016). Mitochondrial Dynamics in Visual Cortex Are Limited In Vivo and Not Affected by Axonal Structural Plasticity. Curr. Biol. *26*, 2609–2616.

Smith, H.L., Bourne, J.N., Cao, G., Chirillo, M.A., Ostroff, L.E., Watson, D.J., and Harris, K.M. (2016). Mitochondrial support of persistent presynaptic vesicle mobilization with age-dependent synaptic growth after LTP. Elife *5*, e15275.

Song, D.H., Park, J., Maurer, L.L., Lu, W., Philbert, M.A., and Sastry, A.M. (2013). Biophysical significance of the inner mitochondrial membrane structure on the electrochemical potential of mitochondria. Phys. Rev. E. Stat. Nonlin. Soft Matter Phys.

Sood, A., Jeyaraju, D.V., Prudent, J., Caron, A., Lemieux, P., McBride, H.M., Laplante, M., Toth, K., and Pellegrini, L. (2014). A Mitofusin-2-dependent inactivating cleavage of Opa1 links changes in mitochondria cristae and ER contacts in the postprandial liver. Proc. Natl. Acad. Sci. U. S. A. *111*, 16017–16022.

Strohm, E., and Daniels, W. (2003). Ultrastructure meets reproductive success: performance of a sphecid wasp is correlated with the fine structure of the flight-muscle mitochondria.

Sun, T., Qiao, H., Pan, P.Y., Chen, Y., and Sheng, Z.H. (2013). Motile axonal mitochondria contribute to the variability of presynaptic strength. Cell Rep.

Takács, V.T., Szőnyi, A., Freund, T.F., Nyiri, G., and Gulyás, A.I. (2015). Quantitative ultrastructural analysis of basket and axo-axonic cell terminals in the mouse hippocampus. Brain Struct. Funct.

Toussaint, C., and Kugler, P. (1989). Anatomy and Embryology Morphometric analysis of mitochondria and boutons in the dentate gyrus molecular layer of aged rats. Anat Embryol *179*, 411–414.

Verstreken, P., Ly, C. V., Venken, K.J.T., Koh, T.W., Zhou, Y., and Bellen, H.J. (2005). Synaptic mitochondria are critical for mobilization of reserve pool vesicles at Drosophila neuromuscular junctions. Neuron.

Völgyi, K., Gulyássy, P., Háden, K., Kis, V., Badics, K., Kékesi, K.A., Simor, A., Györffy, B., Tóth, E.A., Lubec, G., et al. (2015). Synaptic mitochondria: A brain mitochondria cluster with a specific proteome. J. Proteomics.

Wilson, D.F., Harrison, D.K., and Vinogradov, A. (2014). Mitochondrial cytochrome c oxidase and control of energy metabolism: measurements in suspensions of isolated mitochondria. J. Appl. Physiol. *117*, 1424–1430.